Implantable Composite Fibres with Self-supplied H_2O_2 for Localized Chemodynamic Therapy

Gang Wang [a, 1], Jiayu Gao [b, 1], Yike Fu [a, 1], Zhaohui Ren [a], Jie Huang [c], Xiang Li [a, *], Gaorong Han [a, *]

[a] State Key Laboratory of Silicon Materials, School of Materials Science and Engineering, Zhejiang University, Hangzhou, Zhejiang 310027, China

[b] [1]The Affiliated Stomatology Hospital, Zhejiang University School of Medicine, [2]Key Laboratory of Oral Biomedical Research of Zhejiang Province

[c] Mechanical Engineering, University College London, London, UK WC1E 7JE

[1] Authors with equal contribution

* Corresponding Author: xiang.li@zju.edu.cn (XL), hgr@zju.edu.cn (GRH)

Abstract

The anticancer efficacy of chemodynamic therapy (CDT) is considerably restrained by the inadequate content of H_2O_2 within tumor microenvironment (TME), unexpected oxidation of Fenton agents and low targeting efficiency of particulate therapeutic platforms. Herein for the first time, an implantable CDT platform was designed and synthesized by combining Fe^0 nanocrystal embedded mesoporous silica nanoparticles (FeMSN) and PCL-gelatin fibres (PG fibres), denoted as FeMSN@PG fibres. FeMSN was fabricated via in situ reduction of ferrous ions within the mesopores of MSNs, and assembled at the surface of electrospun PG fibres by electrostatic interaction to form a fibrous mesh. The findings reflected that, in an acid condition, FeMSN nanoparticles can liberate from the composite fibres, and be effectively uptaken by 4T1 cancer cells. The FeMSN released may react with oxygen to generate H_2O_2 when the solution pH value was set 6, and subsequently transform the H_2O_2 to intracellular hydroxyl radicals, inducing enhanced cell-killing effect. By implanting the composite fibres locally at the tumor site of mice, promoted anticancer efficacy was observed with comparison of the intratumorally-injected FeMSN nanoparticles. This study suggests that FeMSN@PG composite fibres can serve as a promising localized PDT platform for effective antitumor purposes, which may spark a series of follow-on investigations for localized cancer therapeutic approach.

Key words: chemodynamic therapy; FeMSN; localized drug delivery system; self-supplied H_2O_2; cancer therapy.

Introduction

Chemodynamic therapy (CDT) is an emerging cancer treatment approach, utilizing in situ Fenton or Fenton-like reactions to produce highly toxic hydroxyl radicals (·OH) at the tumor site [1]. It is known that the tumor microenvironment (TME) is characterized by a low pH value [2], excess H_2O_2 [3] and low catalase activity [4]. Under the mild acid condition in the TME, Fenton agents can release reactive ions and initiate reactions that catalyze H_2O_2 to generate ·OH, triggering ferroptosis of cancer cells [5-7]. Due to neutral condition and low presence of H_2O_2, Fenton reactions are suppressed in normal tissue [8, 9], endowing CDT with the specific responsiveness to TME, high selectivity and improved safety. Nonetheless, even if the intracellular H_2O_2 content may reach 100 μM in cancer cells, endogenous H_2O_2 remains insufficient to achieve satisfactory efficiency of CDT [10, 11]. To supply H_2O_2, in exogenous and sustainable manner, has been considered as a crucial characteristic of CDT agents to promote the expected anticancer efficiency.

With the development of biotechnology and nanomedicine, various nanomaterials including iron-based inorganic materials [12-17], and metal-organic framework (MOF) nanomaterials [18, 19] have been investigated for CDT approaches. Iron oxide nanoparticles (IO NPs) [20], iron hydroxides, antiferromagnetic pyrite [21] have been introduced as CDT agents. However, the leakage of ferrous ions during blood circulation, oxidation of ferrous ions (Fe^{2+}) to less reactive ferric ions (Fe^{3+}), and low target efficiency are among the severe limits of current iron-based nanomaterials. Zero valent iron nanoparticles (nZVIs) can react with H_2O and O_2 to produce Fe^{2+} and H_2O_2 under acid condition [22], and has been extensively studied in sewage treatment and soil remediation [23, 24]. Because of the reactive nature of metallic glass, Zhang et al. synthesized amorphous Fe^0 nanoparticles (AFeNPs) for CDT [25]. It was demonstrated that the Fe^{2+} release rate of AFeNPs was more rapid than that of Fe^0 nanocrystals in mild acid conditions. The in vivo study showed that tumor growth was inhibited by the endogenous stimuli-responsive generation of ·OH by AFeNPs. Yu et al. fabricated an FePt alloy nanoparticle for in situ chemodynamic therapy and MRI imaging [26]. Due

to the low pH in tumor cells, the FePt alloy nanoparticles could generate Fe^{2+}, which then catalyze H_2O_2 to hydroxyl radicals and further induce cell death. However, as an extremely reactive metal substance, Fe^0 nanoparticles are prone to react with oxidants such as oxygen in the circumstance. A shell composed of iron oxide or iron hydroxide is consequently formed on the surface of bare nZVIs, and highly suppress the release rate of Fe^{2+} ions. Moreover, bare nZVIs tend to agglomerate, forming a necklace-like structure, which prevents the cell uptake of nZVIs [27]. More importantly, intrinsic shortcomings of systemic drug delivery systems (SDDSs), including failure to target cancer cells, clearance by metabolism and oxidation during blood circulation, can limit the CDT efficiency remarkably when using nZVIs.

Localized drug delivery systems (LDDSs) have been proposed as an alternative platform to address the low delivery efficiency (~ 0.7%) [28], high toxicity to normal tissue [29] and inferior release administration of systemic drug delivery systems (SDDSs) [30]. Current LDDSs are in the form of films, hydrogels, drug-eluting wafers, microarrays and rods. Among these LDDSs, electrospun nanofibres possess unique properties such as high surface area [31], high porosity [32] and desirable biodegradability [33]. Implanted by minimally invasive surgery, LDDSs provide the tumor site with a high concentration of therapeutic factors for a prolonged time while maintaining the systemic drug concentration at a lower level. Particle-embedded electrospun nanofibres combine functional particles and carrier fibres by a particle-electrospinning method [34-36]. For example, photothermal agents such as GNRs [37], CuS_2 [38] and GO nanosheets [39] incorporated in fibres matrices have shown excellent photothermal anticancer performance. However, particles tend to agglomerate in the polymer precursors, and thus induce an unstable electrospinning process [40]. Moreover, with the increase in concentration of nanoparticles, which are often surface-charged, the stability of the Taylor cone during electrospinning process is compromised. After implantation, the particle and drug release rate are highly dependent on the slow degradation of the fibrous matrix, which may consequently limit the therapeutic efficacy.

Nanofibrous mesh with surface assembled therapeutic nanoparticles has recently emerged as a new type of LDDSs with enhanced particle loading efficiency and improved drug release performance. The hierarchical nanoparticle-nanofibres structure endows the system with the advantage of loading therapeutic agents on both components. Since 2017, a photothermal electrospun nanofibres membrane (PGC nanofibres) combined with photoluminescence mesoporous silica nanoparticles (PLMSN) for localized cancer chemotherapy has been developed [41]. Irradiation with 808 NIR, the PLMSN@PGC composite fibres liberated PLMSNs and induced a high cell uptake rate of up to 37.5%. Inspired by the findings, LDDSs may potentially serve as an effective PDT platform to deliver Fenton agents at the tumor site, but no relevant investigations have been reported so far.

Therefore, in this study, an implantable CDT platform was designed and synthesized by combining Fe^0 nanocrystal embedded mesoporous silica nanoparticles (FeMSN) and PCL-Gelatin fibres (PG fibres), denoted as FeMSN@PG fibres (**Fig. 1**). FeMSN was fabricated via in situ reduction of ferrous ions within the mesopores of MSN, and assembled at the surface of electrospun PG fibres via electrostatic interaction to form a fibrous mesh. In an acid condition, FeMSN nanoparticles can liberate from the composite fibres, and be effectively uptaken by 4T1 cancer cells and serve as a Fenton agent. The intracellular FeMSN may react with oxygen to generate H_2O_2, and subsequently induce hydroxyl radicals, enabling significantly enhanced cell-killing effect. By implanting the composite fibres locally at the tumor site of mice, promoted anticancer efficacy was observed with comparison of the intratumorally-injected FeMSN nanoparticles. This study suggests that FeMSN@PG composite fibres can serve as a promising localized PDT platform for effective antitumor purposes.

Experimental Details

Materials

Poly(ε-caprolactone) (PCL, M_w = 70 000 – 90 000), hexadecyltrimethylammonium bromide (CTAB, ≥ 99%), sodium borohydride ($NaBH_4$, ≥ 98.0%) were obtained from

Sigma-Aldrich (St.Louis, MO, USA). Gelatin (type B from bovine skin), Tetraethyl orthosilicate (TEOS), aminopropyltriethoxysilane (APTES, AR), triethanolamine ($C_6H_{15}NO_3$, AR), cyclohexane (C_6H_6, AR), ethanol (AR) were acquired from Sinopharm Chemical Reagent Co., Ltd (Shanghai, China). 2, 2, 2-trifluoroethanol (CF_3CH_2OH, ≥ 99.5%), iron sulfate heptahydrade ($FeSO_4 \cdot 7H_2O$, AR, ≥ 99.0%) was purchased from Aladdin Reagents (Shanghai, China). Deionized water was produced by a Heal Force Ultra-Pure Water System.

Synthesis of Fe^0 nanoparticle embedded mesoporous silica nanoparticles (FeMSN)

Mesoporous silica nanoparticles (MSN) were synthesized according to the method previously reported by our group with slight modification [41]. 20 mL of deionized water and 5 mL of ethanol were mixed to form a homogeneous solution. Next, 50 mg of triethanolamine and 0.2 g of hexadecyltrimethylammonium bromide (CTAB) were added and stirred at 60 ^oC for 30 mins. Subsequently, 2 mL of TEOS was added dropwise and stirred at 60 ^oC for 2 hrs. 20 mL of ethanol was added into the white solution and cooled down to the ambient temperature. Finally, the precipitate was centrifuged and washed with water and ethanol several times. After drying at 80 ^oC overnight, the particles were calcined at 550 ^oC for 5 hrs to remove the surfactant template.

FeMSNs were synthesized according to a modified approach as previously reported [42]. In a typical procedure, 0.25 g of MSN was dispersed in 30 mL of cyclohexane under sonication for 10 mins. 200 µL of $FeSO_4$ solution (2.0 M) was then added drop by drop under stirring for 48 hrs. After air-drying at 80 ^oC for 4 hrs, a brownish mixture was obtained. Next, the mixture was re-dispersed in 30 mL of cyclohexane with sonication for 60 mins. 2 M $NaBH_4$ aqueous solution was added dropwise until the mixture turned black. The molar ratio of BH_4^-/Fe^{3+} was 4: 1. After stirring for 30 min, the mixture was centrifuged, washed with ethanol and water for several times. Finally, the FeMSN was dried at 37 ^oC overnight.

Fabrication of FeMSN@PG composite fibres

PCL-Gelatin (PG) fibres were prepared via an electrospinning method as reported previously. Briefly, 1.0 g PCL and 1.0 g gelatin were added to 10 mL of 2, 2, 2-trifluoroethanol and stirred for 12 hrs at 40 ^{o}C to form a homogeneous precursor solution. The precursor solution was then transferred to an electrospinning setup with a single nozzle. The high applied voltage and distance between the nozzle tip and collector were set to 12 kV and 15 cm, respectively. The flow rate was 1.0 mL h^{-1}. The relative humidity was maintained below 50% RH and the temperature was 30 ^{o}C. Finally, the as-spun fibres were dried at 37 ^{o}C overnight to remove the residual solvent. The FeMSNs were assembled onto the surface of the PG fibres via electrostatic interaction. The zeta potential of FeMSN, PG fibres, and FeMSN@PG fibres were measured to uncover the forming mechanism of the composite fibres. Before the examination, FeMSN was dispersed in the aqueous solution using an ultrasonic probe at 100 W for 10 min. Meanwhile, PG and FeMSN@PG fibres were firstly frozen to reduce the flexibility, milled using a pestle and finally dispersed in the aqueous solution with an ultrasonic probe for the zeta potential measurement. In a typical procedure, 20 mg of FeMSNs were dispersed into 20 mL of ethanol by sonication to form a black solution. Then, 20 mg of PG fibre mesh was immersed in the FeMSN solution and stirred for 12 hrs. When the solution turned transparent, the composite fibre mesh was collected and dried at 37 ^{o}C overnight.

Production of H_2O_2 and ·OH and particle release

A classic colorimetric method based on the degradation of methylene blue (MB) was used to quantify the production of the hydroxyl radical (·OH). In brief, 1 mL of FeMSN (1 mg/mL) PBS solution and 4 mL of MB PBS solution (5 μg/mL) were mixed in an Eppendorf and reacted at 37 ^{o}C while shaking at pH = 7.0 and pH = 6.0. After reacting for various lengths of time, the mixture was centrifuged and the UV-Vis spectra of the supernatant were measured to quantitively study the degradation of MB.

To investigate the depletion of O_2 in the reaction system, a dissolved oxygen meter

(JPBJ-608) was used to monitor the dissolved oxygen in the aqueous solution at pH = 6.0. In brief, after equilibrating of the PBS solution (4 mL) at pH = 6.0 for 30 s, 1 mL of FeMSN PBS solution was added and stirred at room temperature for 360 s. In addition, the dissolved oxygen content of PBS solution was examined under the same condition for comparison.

To confirm the generation of hydroxyl radicals, electron spin resonance spectroscopy was examined using 5, 5-Dimethyl-1-pyrroline N-oxide (DMPO) as a spin trap for ·OH. In a dark Eppendorf tube containing 40 μL of DMPO buffer solution (100 mM), the following reaction systems were added respectively: 10 μL FeMSN solution (500 μg/mL) at pH = 7.0, 10 μL H_2O_2 (5 mM) at pH = 6.0, 10 μL FeMSN solution (500 μg/mL) at pH = 6.0, 5 μL FeMSN solution (1000 μg/mL) + 5 μL H_2O_2 (10 mM) at pH = 6.0 and 5 μL FeMSN solution (1000 μg/mL) + 5 μL H_2O_2 (10 mM) at pH = 6.0. The ESR spectra were measured immediately after the reactants were mixed.

Particle release performance from the platform is vital for localized drug delivery system. FeMSN can only release from the PG fibre surface when the electrostatic interaction is broken in an acidic environment. After incubation in an aqueous solution at pH = 6.0 and 6.5 at 37 °C for 12, 24 and 48 hrs, FeMSN@PG composite fibres were examined using a Field Emission Scanning Electron Microscope. To quantify the release content of FeMSN, 2 mg of FeMSN@PG fibres were immersed in a PBS solution at pH=6.0 at 37 ^{o}C under gentle shaking. At various time intervals, the UV-Vis spectrum was measured, and the amount of released FeMSN was calculated by a standard curve of FeMSN. In addition, FeMSN@PG composite fibres were immersed in an aqueous solution at pH = 7.0 for 7 days to examine the particle release profile at neutral condition.

In vitro anticancer efficacy study

Human HL-7702 liver cells were used to study the cytotoxicity of FeMSN composite fibrous mesh. HL-7702 cells were cultured in a DMEM medium with 1% penicillin and

streptomycin and 10% fetal bovine serum in a 37 °C incubator with 5% CO_2. For the cytotoxicity assay, the composite fibrous mesh was cut into pieces of various sizes and irradiated with ultraviolet light overnight. HL-7702 cells were seeded in 24-well culture plates at a density of 5.0×10^4 cells per well and cultured for 24 hrs. Fresh culture media containing FeMSN composite fibres with concentrations of 20 – 400 μg/mL were added and cultured for 24 hrs. The cell viability was quantified with the standard CCK-8 assay compared with the control group.

Murine breast cancer 4T1 cells were used to study the anticancer effect of the FeMSN@PG composite fibrous mesh. 4T1 cells were seeded in 24-well culture plates at a density of 5.0×10^4 cells per well and cultured overnight. Then, fresh culture media containing the following were tested: (i) control: pure culture medium, (ii) FeMSN@PG fibres, (iii) FeMSN@PG fibres with H_2O_2, (iv)FeMSN@PG fibres at pH = 6 and (v) FeMSN@PG fibres with H_2O_2 at pH = 6. After incubation for 24 hrs and 48 hrs, a standard CCK-8 assay was applied to measure the cell viability of each group. FeMSN@PG composite fibres at various concentrations with H_2O_2 at pH = 6 were also used to study the chemodynamic therapy of the composite fibrous mesh. In addition, N-Acetyl Cysteine (NAC, 5 μM, Beyotime), a nontoxic antioxidant, was used to demonstrate ROS-induced cell apoptosis.

To demonstrate the enhanced chemodynamic therapy by self-supplied H_2O_2 of FeMSN@PG fibres, human 4T1 breast cancer cells were seeded and incubated in hypoxia atmosphere (1% O_2) with various samples including: i: pure culture medium, ii: FeMSN@PG fibre, iii: FeMSN@PG fibre with H_2O_2, iv: FeMSN@PG fibre at pH = 6 and v: FeMSN@PG fibre with H_2O_2 at pH = 6for 24 hrs and 48 hrs. The cell viability was measured using a standard CCK-8 assay.

To confirm the apoptosis of 4T1 cells, calcein acetoxymethyl ester (Calcein-AM) and propidium iodide (PI) and flow cytometry was used. After treated with various samples including i: pure culture medium, ii: FeMSN@PG fibre, iii: FeMSN@PG fibre with H_2O_2,

iv: FeMSN@PG fibre at pH = 6 and v: FeMSN@PG fibre with H_2O_2 for 48 h, 4T1 cells were then treated with trypsin and collected for flow cytometry following a standard protocol. As for Calcein-AM and PI co-staining, 4T1 cells were co-stained with a Calcein-AM and PI and observed using a fluorescence microscope (Nexcope, USA)

In vitro anticancer mechanism study

The uptake of FeMSN by 4T1 cells was studied using fluorescent microscope imaging and flow cytometry. FeMSNs were modified with fluorescein isothiocyanate (FITC) for fluorescent imaging. In brief, 100 mg of FeMSN was added to 25 mL ethanol solution containing 1 mL aminopropyltriethoxysilane (APTES) and maintained at 40 ^oC for 24 h for amination. Then FeMSN-NH_2 was modified with carboxylated FITC in dichloromethane solution. The FeMSN-FITC was assembled on surface of PG fibres via electrostatic interaction and used for further study. 4T1 human breast cancer cells were incubated with FeMSN-FITC@PG fibres at pH = 6.0 for 0-24 hours. The cells were then treated with trypsin and collected for flow cytometry. For fluorescent microscope imaging, the cells were stained with diamidino-phenyl-indole (DAPI) and fixed and examined with a fluorescent microscope.

To examine the intracellular O_2 detection, a commercial O_2 sensor, $[Ru(dpp)_3]Cl_2$ (RDPP) [43], was used as a probe to preincubate with 4T1 Human breast cancer cells for 4 h. After washed for 3 times, 4T1 cells were then incubated with different samples including i: pure culture medium, ii: FeMSN@PG fibre, iii: FeMSN@PG fibre with H_2O_2, iv: FeMSN@PG fibre at pH = 6 and v: FeMSN@PG fibre with H_2O_2 at pH = 6 for 12 h. Finally, the cells were rinsed with PBS for several times for fluorescent imaging under a fluorescent microscope. The excitation wavelength was chosen at 488 nm and emission was collected from 600 to 650 nm to examine the fluorescence of RDPP.

The intracellular H_2O_2 concentration was detected using a Hydrogen Assay Kit (Beyotime) [44]. According to the protocol provided by the kit, after incubated with FeMSN@PG fibres at neutral and pH = 6.0 for 12h, 4T1 cells were lysed and

centrifugated for H_2O_2 detection. Subsequently, the supernatants were collected (100 µL) and added with 50 µL reaction reagent for 30 min at room temperature. The emission at 560 nm was measured using a microplate reader (Tecan). The concentration of H_2O_2 was calculated using a standard curve generated using the standard H_2O_2 solution provided by the manufacturer.

To further study the mechanism of the CDT of FeMSN@PG fibres, intracellular ROS production was examined using 2,7-dichlorodi-hydrofluorescein diacetate (DCFH-DA) as a fluorescent probe following the standard protocol. The fluorescent intensity of DCFH at 520 nm (with an excitation at 480 nm) was measured using a confocal microscope.

In vivo Tumor model

In vivo study was performed humanely in compliance with guidelines approved by the animal ethics committee of the Biological Resource Centre of the Agency for Science, Technology and Research, Zhejiang University. Female Balb/c mice (4 weeks old) were purchased from the Zhejiang Academy of Medical Science. To create the tumor model, 50µL of PBS solution with 4T1 cells (2×10^5) were injected subcutaneously into the right axilla of each mouse.

The size (length and width) of tumors were measured, and the volume (V) was calculated as $V = (\text{width}^2 \times \text{length})/2$. The anticancer experiments started when the tumor volume reached 50 mm^3.

Tumor prohibition

Mice previously treated to induce a tumor, were randomly divided into 4 groups (5 mice/group): control (Group 1), PG without FeMSN (Group 2), FeMSN without PG (Group 3), FeMSN @ PG (Group 4). PCL-Gelatin fibres and FeMSN@PG composite fibrous mesh were implanted into the tumor site, respectively, as illustrated in Fig. 4a. The FeMSN solution (50 µL, 10 mg/mL) was injected by intratumoral injection in group

3. As the control, mice in group 1 were injected with 50μL saline solution only. Penicillin was used in all group to prevent infection after surgery. The body weight and tumor size were monitored and measured every day in following 2 weeks. The therapeutic effect was evaluated by measuring the tumor size. On day 14, all the mice were sacrificed, and the tumors were collected.

To further examine the involvement of ROS in cancer treatment with FeMSN@PG fibres, a series of *in vivo* studies were carried out following the similar procedure above. For the mice treated with FeMSN@PG fibres, NAC (PBS solution) was injected at a safe dosage of 100 mg/kg intratumorally once every two days [45]. A group of mice were treated with only intertumorally-injected NAC at the same dosage for comparison.

Surgery procedure

The mice were anesthetized by an intraperitoneal injection of chloral hydrate (1 mg/330 g). After exposure of tumor, PG fibres (1mg) and FeMSN@PG fibrous membranes (1 mg) were implanted at the surface of the tumor in groups 2 and 4 respectively. The total amount of FeMSN in group 4 was the same with that in group 3. The skin was closed with sutures using a 5-0 suture line.

Histology examination

After the mice were sacrificed, the tumor tissues from control and treated mice were histologically examined. Four groups of tumors were collected and fixed in 4% paraformaldehyde solution embedded in paraffin using a standard method. H&E staining of the tumor samples was carried out following standard (H&E staining) procedures and the tissue slices were investigated using an inverted microscope system.

To examine the treatment efficacy in vivo, immunofluorescence terminal deoxynucleotidyl transferase-mediated dUTP-biotin nick end labeling (TUNEL) assay and Ki67 staining assay were also conducted. Briefly, after treated with different

samples for 48 h, the tumor tissues from each group of mice were collected, fixed with formalin and embedded by paraffin. The tissues were then cut into slices and stained following the manufacturer's instruction of In Situ Cell Death Detection Kit (ROCHE). For Ki67 staining, the tumor tissues were stained following the standard protocol of Ki-67 staining. The tissue slices were observed by a confocal microscopy.

Statistical analysis

All data in this article is expressed as a mean ± SD, and all comparison results between experimental groups were calculated through Student's t-test. Variations in the data were considered to be significant when ***$p < 0.001$, **$p < 0.01$ or *$p < 0.05$.

Characterization

The morphology, microstructure and composition of MSN, FeMSN, PG fibres and FeMSN@PG fibres were investigated by a Hitachi SU-70 field-emission scanning electron microscope (FESEM) and a FEI Tecnai F20 high-resolution transmission electron microscope (HRTEM). Fourier Transform Infrared Spectroscopy (FTIR) spectra were measured on a PerkinElmer 580B (Tensor 27, Bruker) infrared spectrophotometer using the KBr pellet technique. The zeta potential of materials was conducted by a Zetasizer (Zetasizer Nano-ZS, Malvern). UV-vis spectroscopy measurements were recorded on a TU-1810 UV-vis spectrophotometer. The X-ray diffraction (XRD) patterns were measured by a thermo ARL X'TRA powder diffractometer. The X-ray photoelectron spectroscopy (XPS) spectra were measured on an AXIS Supra XPS spectroscopy (Kratos). The electron-spin resonance (ESR) spectra were recorded by a Bruker A300 EPR spectroscopy.

Results and Discussion

Synthesis of FeMSN and FeMSN@PG composite fibres

The FeMSN was synthesized by a modified two-step approach. As illustrated in Fig. 2a, the MSNs prepared were immersed in the Fe^{2+} precursor for a certain period of time, allowing the diffusion of Fe^{2+} ions. After the reduction using $NaBH_4$ aqueous solution,

Fe^0 crystals were formed within the mesopores of MSNs, to form FeMSN. The nanoparticles prepared were then assembled at the surface of electrospun PG fibres to form the composite fibres. The as-prepared MSNs were of uniform sphere form with an average diameter of ~78 nm (Fig. 2b, Fig. S1). Typical wormhole mesostructures can be observed clearly. After the incorporation of nano zero valent irons (nZVIs), the average diameter of FeMSN was barely changed (~91 nm) (Fig. S1) while the contrast of TEM image became darker, and the mesopores of MSNs disappeared (Fig. 2c), suggesting that nZVIs were successfully embedded in the mesoporous channels of MSNs. Meanwhile, EDS element mapping images show a homogeneous distribution of iron within the MSN matrix (Fig. 2d), confirming the formation of FeMSN. Both MSN and FeMSN presented a broad peak centered at 23.5^o (Fig. 2e), which is attributed to the amorphous phase of silica. A diffraction peak at 44.6^o corresponding to Fe^0 (JCPDS No. 06-0696) could be observed in the XRD pattern of FeMSN. Compared to that in the nZVI@MSN reported previously [42], the peak of Fe^0 was sharper, owing to highly crystalline nZVIs embedded. Moreover, Fe peak with a low magnitude appeared in the XPS pattern of FeMSN (Fig. 2f), revealing that nZVIs were loaded within the channels of MSN matrix. The oxidation of nZVIs in the presence of oxygen has been a challenging limit for its biomedical applications. In the study, the MSN matrix can potentially protect the nZVIs embedded from oxidation in air or aqueous solution, paving the way to the further investigations.

The FeMSN@PG composite fibres were fabricated by combining PCL-Gelatin (PG) fibres and FeMSNs via electrostatic interaction. As shown in Fig. 2i, electrospun PG fibres presented smooth surface with a diameter of ~1 μm. The zeta potentials of as-prepared PG fibres and FeMSNs were -29.7 mV and 6.1 mV, respectively (Fig. 2h), implying the feasibility to assemble FeMSNs on the surface of PG fibres by electrostatic effect. After immersing PG fibres in a FeMSN solution for 12 hrs, the colour of fibres membrane turned from white to black (Fig. S2). The SEM image of FeMSN@PG fibres showed that high content of FeMSNs were assembled at the surface of PG fibres, inducing the coarse surface of fibres (Fig. 2j). The band located at 618 cm^{-1} in the FTIR

spectrum of FeMSN@PG fibres are attributed to the Fe-O vibration of nZVIs (Fig. 2g) [46], and Fe element distributes across the entire FeMSN@PG fibrous mesh (Fig. S3), indicating the successful formation of FeMSN@PG composite fibres. The loading efficiency of Fe^0 nanocrystals in MSN was quantified to be ~29.50 wt%, which is 7 times higher than that previously reported (Table 1) [42].

FeMSN liberation and hydroxyl radical induction

The particle liberation is a crucial characteristic of LDDSs in a particle-fibre form. To investigate the efficiency of FeMSN liberation, FeMSN@PG fibres were immersed in an aqueous solution of pH = 6 at 37 ^oC for 48 hrs. As shown in SEM images and quantified by UV-vis absorption spectra of aqueous solutions, approximately ~58% of the FeMSNs were released from the surface of composite fibres after 12 hrs. After incubation for 48 hrs, about ~91% of FeMSNs were liberated which would potentially facilitate the therapeutic performance of the FeMSN@PG fibrous mesh (Fig. 3a, S4 and S5). In comparison, the release of FeMSNs was much slower when the pH increased to 6.5 and 7.0 (Fig. S6).

Encouraged by the favorable dispersity and effective liberation of FeMSNs, the generation of hydroxyl radicals by FeMSNs was then explored. Methylene blue (MB) was used as a colorimetric probe to quantify the production of ·OH (Fig. S7). When the solution pH was set at 6, the removal efficiency of MB reached ~77% within 15 mins with the concentration of FeMSN at 200 μg/mL, while less than ~10% of MB was degraded when the pH value increased to 7 (Fig. 3b-d). In addition, with the addition of FeMSN (100 μg/mL) at pH = 6.0, the depletion of dissolved oxygen occurred immediately , showing 1.63 mg/mL decrease of dissolved O_2 within 360 seconds (**Fig. S8**). The mechanism is that, under an acidic condition, the Fe^{2+} release rate is higher than that in neutral condition. Along with the release of ferrous ions, H_2O_2 is produced through the reaction between Fe^0, oxygen and hydrogen ions, following the Equation 1.

$$2Fe^0 + O_2 + 2H^+ = Fe^{2+} + H_2O_2 \text{ (Equation 1)}$$

The reaction products, Fe^{2+} and H_2O_2, serve as Fenton agents for the MB degradation, following the reactions of Equation 2 and 3.

$$Fe^0 + H_2O_2 + H^+ = Fe^{2+} + 2H_2O \text{ (Equation 2)}$$

$$Fe^{2+} + H_2O = Fe^{3+} + OH^- + \cdot OH \text{ (Equation 3)}$$

ESR was conducted to confirm the radicals formed during the reactions above. As shown in Fig. 3e, no ESR signals presented when FeMSN was added into the solution with pH of 7. However, characteristic peaks of hydroxyl radicals, with intensity ratio of 1:2:2:1, appeared when the solution pH was decreased to 6. After adding extra content of H_2O_2, the ESR signal intensity of all peaks became stronger, as expected. In addition, it was found that lower pH may induce the increased content of hydroxyl radicals (Fig. 3d). Taking advantage of the reaction with oxygen under acidic condition of TEM, FeMSNs can potentially serve as a bio-responsive and self-supplied H_2O_2 PDT platform.

In vitro study

The in vitro anticancer performance of FeMSN@PG fibres was examined using mouse 4T1 breast cancer cells and Human HL-7702 liver cells. No clear toxicity to 7702 cells was observed when cultured with FeMSN@PG fibres up to 400 μg/mL, implying its expected cyto-compatibility (Fig. 4a). Subsequently, 4T1 cells were seeded and incubated with FeMSN@PG fibres at pH = 6. As shown in Fig. 4b, ~79% of 4T1 cancer cells were killed after being incubated with 400 μg/mL fibres for 48 hrs. To further investigate the in vitro anticancer properties of FeMSN@PG fibres, 4T1 cancer cells were incubated with different groups of samples, including (i) pure culture medium, (ii) FeMSN@PG fibres, (iii) FeMSN@PG fibres with H_2O_2, (iv) FeMSN@PG fibres at pH = 6 and (v) FeMSN@PG fibres with H_2O_2 at pH = 6. To simulate the low pH value and overproduced H_2O_2 of TME, safe dosages of 100 μM HCl and H_2O_2 were added to the culture medium (Fig. S9). As shown in Fig. 4c, after incubation with FeMSN@PG fibres for 48 hrs, cell viability decreased from ~35% (group iv) to ~19% (group v) due to the addition of H_2O_2, reflecting its superior in vitro anticancer effect. In contrast, with the

addition of NAC (5 μM), the cell viability increased to ~74% and ~45% for 24 h and 48 h, respectively (Fig. S10). The cell viability decreased by a marginal magnitude in group ii and iii after 24 hrs. This in attributed to the passive particle liberation of FeMSN@PG fibres in the neutral condition. The in vitro anticancer effect to 4T1 cells were further confirmed by flow cytometry, calcein-AM and PI co-staining (Fig. S11, Fig. S12). Approximately ~86 % of 4T1 cells were dead after being treated with FeMSN@PG fibre and H_2O_2 (100 μM) at pH = 6.0, while only ~5% of cells death in the control group presented (Fig. S12).

The cellular uptake phenomenon of FeMSN released from the composite fibres was examined using a fluorescent microscope and flow cytometry. With the increase of incubating time, the green fluorescence of FITC in 4T1 cells increased, indicating the particle internalization by 4T1 cells (Fig. S13). This result was further confirmed and quantified via flow cytometry. After incubation for 6 h, 12 h and 24 h, the cell uptake rates were 3.90%, 10.14% and 14.30%, respectively (Fig. S14). Therefore, under acidic condition, H^+ ions are absorbed by negative surface of FeMSN and the electrostatic interaction between FeMSN and PG fibres is weakened. FeMSNs release from the surface of PG fibres. With the increased incubation time, more FeMSNs were released and uptaken by cells, resulting in the increase of green fluorescence of 4T1 cells.

To uncover the mechanism of the strong cell-killing effect achieved by FeMSN@PG fibres, 2',7'-dichlorofluorescein diacetate (DCFH-DA) was used to examine the ROS induction within cancer cells. After treatment with FeMSN@PG fibres for 6 hrs in an acidic culture media, 4T1 cells were stained with DAPI and DCFH-DA. Low content of ROS was generated in the sample groups i and ii, whereas bright green fluorescence was observed in group iv (Fig. 4d). A commercial O_2 sensor, $[Ru(dpp)_3]Cl_2$ (RDPP, J&K Scientific), was used as a probe to detect the depletion of intracellular O_2. No fluorescence was observed in the groups incubated at neutral pH condition due to the quenching of RDPP by O_2. In contrast, 4T1 cells treated with FeMSN@PG cells at pH = 6.0 (Group iv and v) demonstrated strong fluorescence, indicating the intracellular

depletion of O_2 induced by FeMSN uptaken (Fig. S15). In addition, the intracellular H_2O_2 concentration was detected using a Hydrogen Assay Kit (Beyotime). Compared with the control group, an increase by ~17% of intracellular H_2O_2 concentration presented for cells incubated with FeMSN@PG fibres at pH = 6.0, indicating the self-supply property of H_2O_2 by FeMSN released (Fig. S16). The findings reflect that FeMSN can react with oxygen to produce hydroperoxide, and subsequently catalyze to form hydroxyl radicals. In contrast, in the hypoxia condition, the cell viability increases to 85% and 68% for 24 h and 48 h, respectively (Fig. S17). The result indicates that, with low oxygen supply, Fe^0 could not effectively react with O_2 and H^+ ions to produce Fe^+ and H_2O_2. Thus, less hydroxyl radicals are generated to induce cell death. When adding additional H_2O_2 to the culture media, the green fluorescence was enhanced owing to sufficient supply of reactants to induce ROS, enabling the promoted cell necrosis, as expected (Fig. 3e).

In vivo study of FeMSN composite fibres

The in vivo anticancer efficiency of FeMSN@PG fibres were evaluated using the 4T1 mouse tumor model. PG fibres and FeMSN@PG fibres were implanted at the tumor sites following the surgery procedures, including exposure, implantation and suture, demonstrated in Fig. 5a. Solution containing free FeMSNs were directly injected intratumorally, as a comparison. The mice body weight and tumor size were monitored during the 14-day test period. Compared with the blank control group, the tumors in mice that had received pure PG-fibre implantation presented a similar growth rate. For the mice injected with FeMSNs, tumor growth was partially delayed (Fig. 5b). In contrast, for the mice received FeMSN@PG implantation, the tumor size noticeably shrunk from day 3 after surgery, and the tumor growth was considerably inhibited for the following 14 days. No appreciable body weight variation was observed for all mice groups (Fig. 5c), indicating no clear negative effect to mice was induced by all samples. Photographs of the tumors collected from representative mice are shown in Fig. 5d, visually displaying the tumor growth progress over 14 days. The results indicate that FeMSN@PG significantly inhibited tumor growth despite the short-term increase in

tumor size, which may be attributed to the mild chronic inflammatory response of the material that commonly occurs after implantation. In addition, tumors in the FeMSN@PG group swelled and turned dark, and then shrank and hardened gradually over time. Photographs of mice after several days of treatment further confirmed the anticancer efficiency of FeMSN@PG fibres (Fig. S18). In addition, compared with the blank control group, the tumor growth in mice treated with FeMSN@PG and NAC were hardly delayed (Fig. S19).

Prussian Blue could visually demonstrate iron ions in tissues. As shown in Fig. S20, tumor specimen treated with FeMSN@PG fibres for 2 days presented a dark blue ribbon, implying that FeMSN could liberate from PG fibres and uptaken by cancer cells. Furthermore, H&E staining, TUNEL assay and Ki67 staining assay were conducted to demonstrate the treatment efficacy of FeMSN@PG fibres. H&E-stained micrographs of the tumor specimen after FeMSN@PG implantation showed the enhanced damage compared to that of FeMSN injection while the cells in the control and PG implantation groups retained their regular morphology (Fig. 5e). Only marginal proportion of tumor tissue present apoptotic signals in the control group and PG-fibre implantation group. For the group treated with implanted FeMSN@PG fibres, approximately half of the tumor tissue shows strong apoptotic signals while the group received i.t. FeMSN injection indicates much less apoptotic signals, demonstrating the promoted treatment efficacy by FeMSN@PG fibres than FeMSN injection (Fig. S21). This was further confirmed by the fluorescent images of Ki67 staining after treatment with FeMSN@PG fibres (Fig. S22). However, the apoptotic signals sharply decreased due to the injection of N-acetyl cysteine (NAC), a nontoxic antioxidant for ROS clearance, suggesting that intracellular ROS induced played an important role in the treatment by FeMSN@PG fibres.

Conclusions

In this study, for the first time, an implantable CDT platform was designed and synthesized by combining Fe^0 nanocrystal embedded mesoporous silica nanoparticles

and PCL-Gelatin fibres (FeMSN@PG). FeMSN was fabricated via in situ reduction of ferrous ions within the mesopores of MSNs, and assembled at the surface of electrospun PG fibres via electrostatic interaction to form a fibrous mesh. It was found that, in an acid condition, FeMSN nanoparticles can liberate from the composite fibres, and be effectively uptaken by 4T1 cancer cells. The FeMSN released reacts with oxygen to generate H_2O_2 in an acid condition, and subsequently transforms the H_2O_2 to intracellular hydroxyl radicals, inducing significantly enhanced cell-killing effect. By implanting the composite fibres locally at the tumor site of mice, promoted antitumor efficacy was achieved with comparison of the intratumoral-injected FeMSN nanoparticles. This study suggests that FeMSN@PG composite fibres may serve as a potential localized CDT platform for effective antitumor purposes, which may inspire future explorations for cancer therapeutic technology with feasibility and high efficacy.

Acknowledgement

This work was financially supported by the National Natural Science Foundation of China (51672247), the '111' Program funded by Education Ministry of China and State Bureau of Foreign Experts Affairs (B16043), Fundamental Research Funds for Central Universities (2019xzzx005-3-01) and the Provincial Key Research Program of Zhejiang Province (2020C04005).

Reference

[1] Z. Tang, Y. Liu, M. He, W. Bu, Chemodynamic Therapy: Tumour Microenvironment-Mediated Fenton and Fenton-like Reactions, Angewandte Chemie, 58 (2019) 946-956.

[2] R.A. Gatenby, R.J. Gillies, Why do cancers have high aerobic glycolysis?, Nature reviews. Cancer, 4 (2004) 891-899.

[3] Q. Chen, C. Liang, X. Sun, J. Chen, Z. Yang, H. Zhao, L. Feng, Z. Liu, H2O2-responsive liposomal nanoprobe for photoacoustic inflammation imaging and tumor theranostics via in vivo chromogenic assay, Proc Natl Acad Sci U S A, 114 (2017) 5343-5348.

[4] M. Nishikawa, A. Tamada, H. Kumai, F. Yamashita, M. Hashida, Inhibition of experimental pulmonary metastasis by controlling biodistribution of catalase in mice, International Journal of Cancer, 99 (2002) 474-479.

[5] P. Ma, H. Xiao, C. Yu, J. Liu, Z. Cheng, H. Song, X. Zhang, C. Li, J. Wang, Z. Gu, J. Lin, Enhanced Cisplatin Chemotherapy by Iron Oxide Nanocarrier-Mediated Generation of Highly Toxic Reactive Oxygen Species, Nano letters, 17 (2017) 928-937.

[6] G. Huang, H. Chen, Y. Dong, X. Luo, H. Yu, Z. Moore, E.A. Bey, D.A. Boothman, J. Gao, Superparamagnetic iron oxide nanoparticles: amplifying ROS stress to improve anticancer drug efficacy, Theranostics, 3 (2013) 116-126.
[7] Y. Dai, Z. Yang, S. Cheng, Z. Wang, R. Zhang, G. Zhu, Z. Wang, B.C. Yung, R. Tian, O. Jacobson, C. Xu, Q. Ni, J. Song, X. Sun, G. Niu, X. Chen, Toxic Reactive Oxygen Species Enhanced Synergistic Combination Therapy by Self-Assembled Metal-Phenolic Network Nanoparticles, Adv Mater, 30 (2018).
[8] M.P. Murphy, How mitochondria produce reactive oxygen species, The Biochemical journal, 417 (2009) 1-13.
[9] S. Zhai, X. Hu, Y. Hu, B. Wu, D. Xing, Visible light-induced crosslinking and physiological stabilization of diselenide-rich nanoparticles for redox-responsive drug release and combination chemotherapy, Biomaterials, 121 (2017) 41-54.
[10] Y. Liu, X. Ji, W.W.L. Tong, D. Askhatova, T. Yang, H. Cheng, Y. Wang, J. Shi, Engineering Multifunctional RNAi Nanomedicine To Concurrently Target Cancer Hallmarks for Combinatorial Therapy, Angewandte Chemie, 57 (2018) 1510-1513.
[11] S. Wang, Z. Wang, G. Yu, Z. Zhou, O. Jacobson, Y. Liu, Y. Ma, F. Zhang, Z.Y. Chen, X. Chen, Tumor-Specific Drug Release and Reactive Oxygen Species Generation for Cancer Chemo/Chemodynamic Combination Therapy, Advanced science, 6 (2019) 1801986.
[12] H. Bi, Y. Dai, P. Yang, J. Xu, D. Yang, S. Gai, F. He, B. Liu, C. Zhong, G. An, J. Lin, Glutathione Mediated Size-Tunable UCNPs-Pt(IV)-ZnFe2 O4 Nanocomposite for Multiple Bioimaging Guided Synergetic Therapy, Small, 14 (2018) e1703809.
[13] K.-T. Lee, Y.-J. Lu, F.-L. Mi, T. Burnouf, Y.-T. Wei, S.-C. Chiu, E.-Y. Chuang, S.-Y. Lu, Catalase-Modulated Heterogeneous Fenton Reaction for Selective Cancer Cell Eradication: SnFe2O4 Nanocrystals as an Effective Reagent for Treating Lung Cancer Cells, ACS Applied Materials & Interfaces, 9 (2017) 1273-1279.
[14] D. Wang, J. Zhou, R. Chen, R. Shi, G. Xia, S. Zhou, Z. Liu, N. Zhang, H. Wang, Z. Guo, Q. Chen, Magnetically guided delivery of DHA and Fe ions for enhanced cancer therapy based on pH-responsive degradation of DHA-loaded Fe3O4@C@MIL-100(Fe) nanoparticles, Biomaterials, 107 (2016) 88-101.
[15] Q. An, C. Sun, D. Li, K. Xu, J. Guo, C. Wang, Peroxidase-like activity of Fe3O4@carbon nanoparticles enhances ascorbic acid-induced oxidative stress and selective damage to PC-3 prostate cancer cells, ACS Appl Mater Interfaces, 5 (2013) 13248-13257.
[16] L. Wang, M. Huo, Y. Chen, J. Shi, Iron-engineered mesoporous silica nanocatalyst with biodegradable and catalytic framework for tumor-specific therapy, Biomaterials, 163 (2018) 1-13.
[17] A.D. Bokare, W. Choi, Review of iron-free Fenton-like systems for activating H2O2 in advanced oxidation processes, J Hazard Mater, 275 (2014) 121-135.
[18] D.W. Zheng, Q. Lei, J.Y. Zhu, J.X. Fan, C.X. Li, C. Li, Z. Xu, S.X. Cheng, X.Z. Zhang, Switching Apoptosis to Ferroptosis: Metal-Organic Network for High-Efficiency Anticancer Therapy, Nano letters, 17 (2017) 284-291.
[19] H. Ranji-Burachaloo, F. Karimi, K. Xie, Q. Fu, P.A. Gurr, D.E. Dunstan, G.G. Qiao, MOF-Mediated Destruction of Cancer Using the Cell's Own Hydrogen Peroxide, ACS Appl Mater Interfaces, 9 (2017) 33599-33608.
[20] Z. Zhou, J. Song, R. Tian, Z. Yang, G. Yu, L. Lin, G. Zhang, W. Fan, F. Zhang, G. Niu, L. Nie, X. Chen, Activatable Singlet Oxygen Generation from Lipid Hydroperoxide Nanoparticles for Cancer Therapy, Angewandte Chemie International Edition, 56 (2017) 6492-6496.
[21] Z. Tang, H. Zhang, Y. Liu, D. Ni, H. Zhang, J. Zhang, Z. Yao, M. He, J. Shi, W. Bu, Antiferromagnetic

Pyrite as the Tumor Microenvironment-Mediated Nanoplatform for Self-Enhanced Tumor Imaging and Therapy, Adv Mater, 29 (2017).
[22] D.L. Huber, Synthesis, properties, and applications of iron nanoparticles, Small, 1 (2005) 482-501.
[23] Z. Zhu, Y. Xu, B. Qi, G. Zeng, P. Wu, G. Liu, W. Wang, F. Cui, Y. Sun, Adsorption-intensified degradation of organic pollutants over bifunctional α-Fe@carbon nanofibres, Environmental Science: Nano, 4 (2017) 302-306.
[24] J. Fan, Y. Guo, J. Wang, M. Fan, Rapid decolorization of azo dye methyl orange in aqueous solution by nanoscale zerovalent iron particles, Journal of Hazardous Materials, 166 (2009) 904-910.
[25] C. Zhang, W. Bu, D. Ni, S. Zhang, Q. Li, Z. Yao, J. Zhang, H. Yao, Z. Wang, J. Shi, Synthesis of Iron Nanometallic Glasses and Their Application in Cancer Therapy by a Localized Fenton Reaction, Angewandte Chemie, 55 (2016) 2101-2106.
[26] L. Yue, J. Wang, Z. Dai, Z. Hu, X. Chen, Y. Qi, X. Zheng, D. Yu, pH-Responsive, Self-Sacrificial Nanotheranostic Agent for Potential In Vivo and In Vitro Dual Modal MRI/CT Imaging, Real-Time, and In Situ Monitoring of Cancer Therapy, Bioconjugate chemistry, 28 (2017) 400-409.
[27] L. Li, J. Hu, X. Shi, M. Fan, J. Luo, X. Wei, Nanoscale zero-valent metals: a review of synthesis, characterization, and applications to environmental remediation, Environmental science and pollution research international, 23 (2016) 17880-17900.
[28] Y. Fu, X. Li, Z. Ren, C. Mao, G. Han, Multifunctional Electrospun Nanofibres for Enhancing Localized Cancer Treatment, Small, (2018) e1801183.
[29] S. Huang, S. Duan, J. Wang, S. Bao, X. Qiu, C. Li, Y. Liu, L. Yan, Z. Zhang, Y. Hu, Folic-Acid-Mediated Functionalized Gold Nanocages for Targeted Delivery of Anti-miR-181b in Combination of Gene Therapy and Photothermal Therapy against Hepatocellular Carcinoma, Adv. Funct. Mater., 26 (2016) 2532-2544.
[30] Y. Fu, X. Chen, X. Mou, Z. Ren, X. Li, G. Han, A Dual-Color Luminescent Localized Drug Delivery System with Ratiometric-Monitored Doxorubicin Release Functionalities, ACS Biomaterials Science & Engineering, 2 (2016) 652-661.
[31] J. Xue, J. Xie, W. Liu, Y. Xia, Electrospun Nanofibres: New Concepts, Materials, and Applications, Accounts of chemical research, 50 (2017) 1976-1987.
[32] S. Jiang, L.P. Lv, K. Landfester, D. Crespy, Nanocontainers in and onto Nanofibres, Accounts of chemical research, 49 (2016) 816-823.
[33] L.S. Nair, S. Bhattacharyya, C.T. Laurencin, Development of novel tissue engineering scaffolds via electrospinning, Expert opinion on biological therapy, 4 (2004) 659-668.
[34] G. Yang, J. Wang, Y. Wang, L. Li, X. Guo, S. Zhou, An Implantable Active-Targeting Micelle-in-Nanofibre Device for Efficient and Safe Cancer Therapy, ACS Nano, 9 (2015) 1161-1174.
[35] Y. He, X. Li, J. Ma, G. Ni, G. Yang, S. Zhou, Programmable Codelivery of Doxorubicin and Apatinib Using an Implantable Hierarchical-Structured Fibre Device for Overcoming Cancer Multidrug Resistance, Small, 15 (2019) e1804397.
[36] X. Li, Y. He, J. Hou, G. Yang, S. Zhou, A Time-Programmed Release of Dual Drugs from an Implantable Trilayer Structured Fibre Device for Synergistic Treatment of Breast Cancer, Small, (2019) e1902262.
[37] M. Cheng, H. Wang, Z. Zhang, N. Li, X. Fang, S. Xu, Gold nanorod-embedded electrospun fibrous membrane as a photothermal therapy platform, ACS Appl Mater Interfaces, 6 (2014) 1569-1575.
[38] X. Wang, F. Lv, T. Li, Y. Han, Z. Yi, M. Liu, J. Chang, C. Wu, Electrospun Micropatterned Nanocomposites Incorporated with Cu2S Nanoflowers for Skin Tumor Therapy and Wound Healing, ACS Nano, 11 (2017) 11337-11349.
[39] N. Mauro, C. Scialabba, G. Pitarresi, G. Giammona, Enhanced adhesion and in situ photothermal

ablation of cancer cells in surface-functionalized electrospun microfibre scaffold with graphene oxide, International journal of pharmaceutics, 526 (2017) 167-177.
[40] A. GhavamiNejad, A.R.K. Sasikala, A.R. Unnithan, R.G. Thomas, Y.Y. Jeong, M. Vatankhah-Varnoosfaderani, F.J. Stadler, C.H. Park, C.S. Kim, Mussel-Inspired Electrospun Smart Magnetic Nanofibres for Hyperthermic Chemotherapy, Adv. Funct. Mater., 25 (2015) 2867-2875.
[41] Y. Li, Y. Fu, Z. Ren, X. Li, C. Mao, G. Han, Enhanced cell uptake of fluorescent drug-loaded nanoparticles via an implantable photothermal fibrous patch for more effective cancer cell killing, J. Mat. Chem. B, 5 (2017) 7504-7511.
[42] H. Lu, C. Wen, S. Gao, Y. Dong, M. Zhang, B. Li, W. Hu, J. Dong, Incorporation of nanoscale zero-valent iron particles in monodisperse mesoporous silica nanospheres: Characterization, reactivity, transport in porous media, Colloids and Surfaces A: Physicochemical and Engineering Aspects, 553 (2018) 28-34.
[43] Z. He, Y. Dai, X. Li, D. Guo, Y. Liu, X. Huang, J. Jiang, S. Wang, G. Zhu, F. Zhang, L. Lin, J.J. Zhu, G. Yu, X. Chen, Hybrid Nanomedicine Fabricated from Photosensitizer-Terminated Metal-Organic Framework Nanoparticles for Photodynamic Therapy and Hypoxia-Activated Cascade Chemotherapy, Small, 15 (2019) e1804131.
[44] S. Xu, X. Yang, Y. Qian, Q. Xiao, Parkinson's disease-related DJ-1 modulates the expression of uncoupling protein 4 against oxidative stress, Journal of neurochemistry, 145 (2018) 312-322.
[45] H. Tian, G. Zhang, H. Li, Q. Zhang, Antioxidant NAC and AMPA/KA receptor antagonist DNQX inhibited JNK3 activation following global ischemia in rat hippocampus, Neuroscience Research, 46 (2003) 191-197.
[46] X. Lv, X. Xue, G. Jiang, D. Wu, T. Sheng, H. Zhou, X. Xu, Nanoscale zero-valent iron (nZVI) assembled on magnetic Fe3O4/graphene for chromium (VI) removal from aqueous solution, Journal of colloid and interface science, 417 (2014) 51-59.

Table List

Table 1 Chemical compositions of FeMSN@PG fibres

Elements	Weight percentage (%wt)	Atomic percentage (%)
C	~37.5	~53.9
O	~30.5	~33.9
Si	~13.6	~8.4
Fe	~12.1	~3.8

Figure List

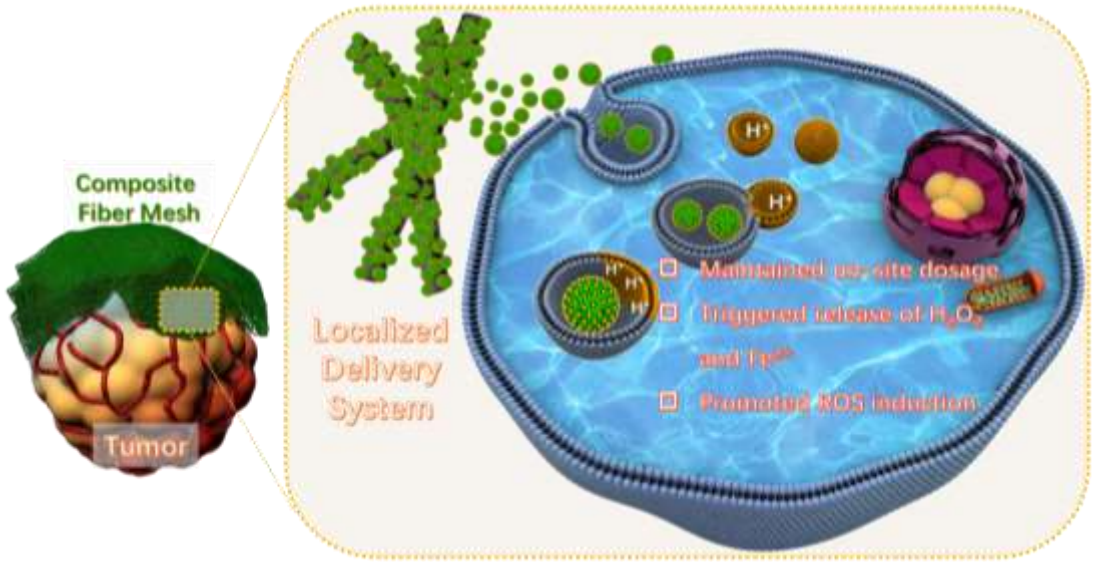

Fig. 1 Schematic illustration of FeMSN@PG fibres for localized PDT approach

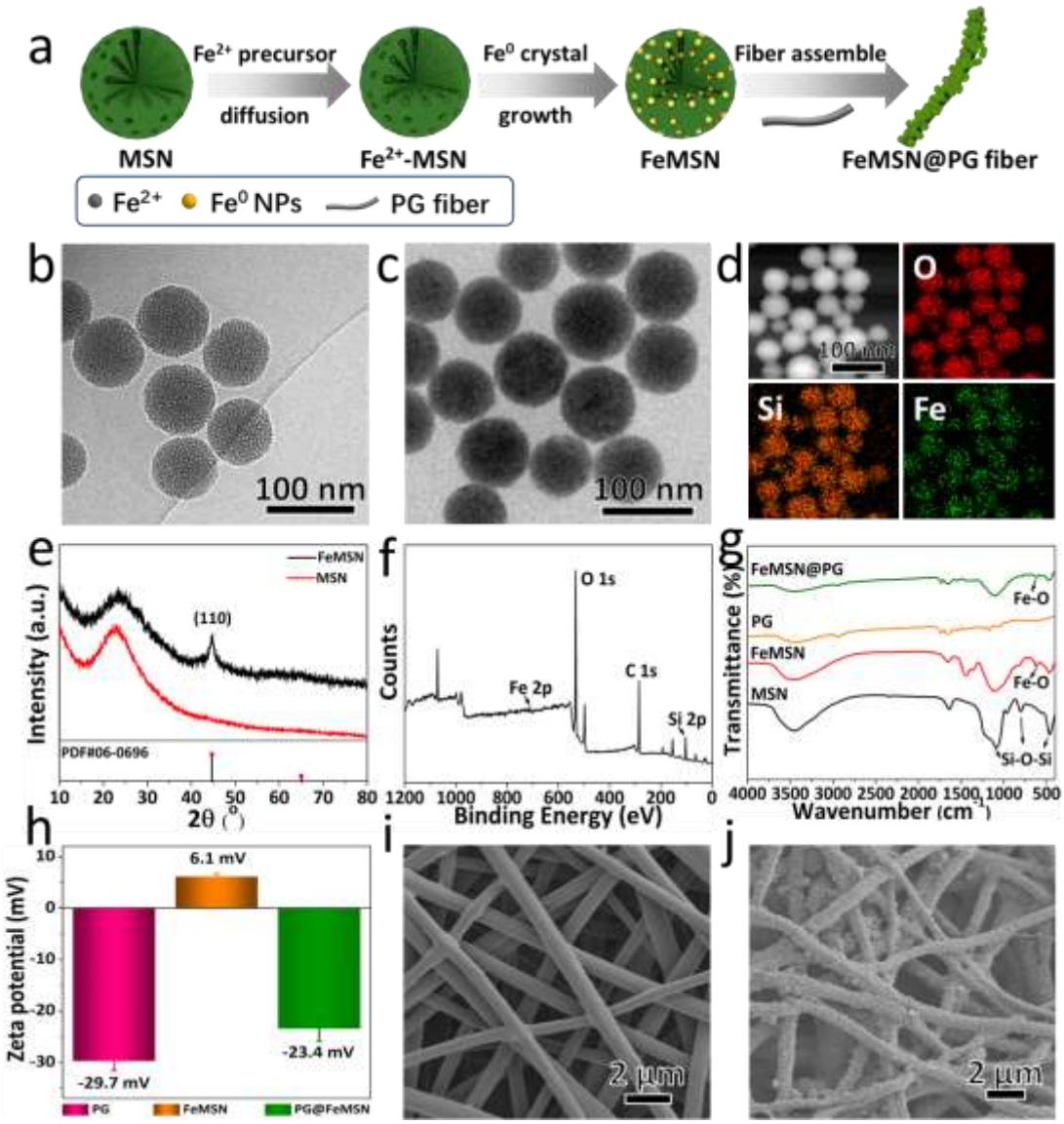

Fig. 2 (a) Schematic illustration of the synthesis of Fe^0 nanocrystal embedded MSN (FeMSN); (b), (c) TEM images of MSN and FeMSN; (d) EDS element distribution mapping images of FeMSN; (e) XRD patterns of FeMSN and MSN; (f) XPS spectrum of FeMSN; (g) FTIR spectra of MSN, FeMSN, PG fibre and FeMSN@PG composite fibre; (h) zeta potentials of FeMSN, PG fibre and FeMSN@PG composite fibre; (i), (j) SEM images of PG and FeMSN@PG fibre.

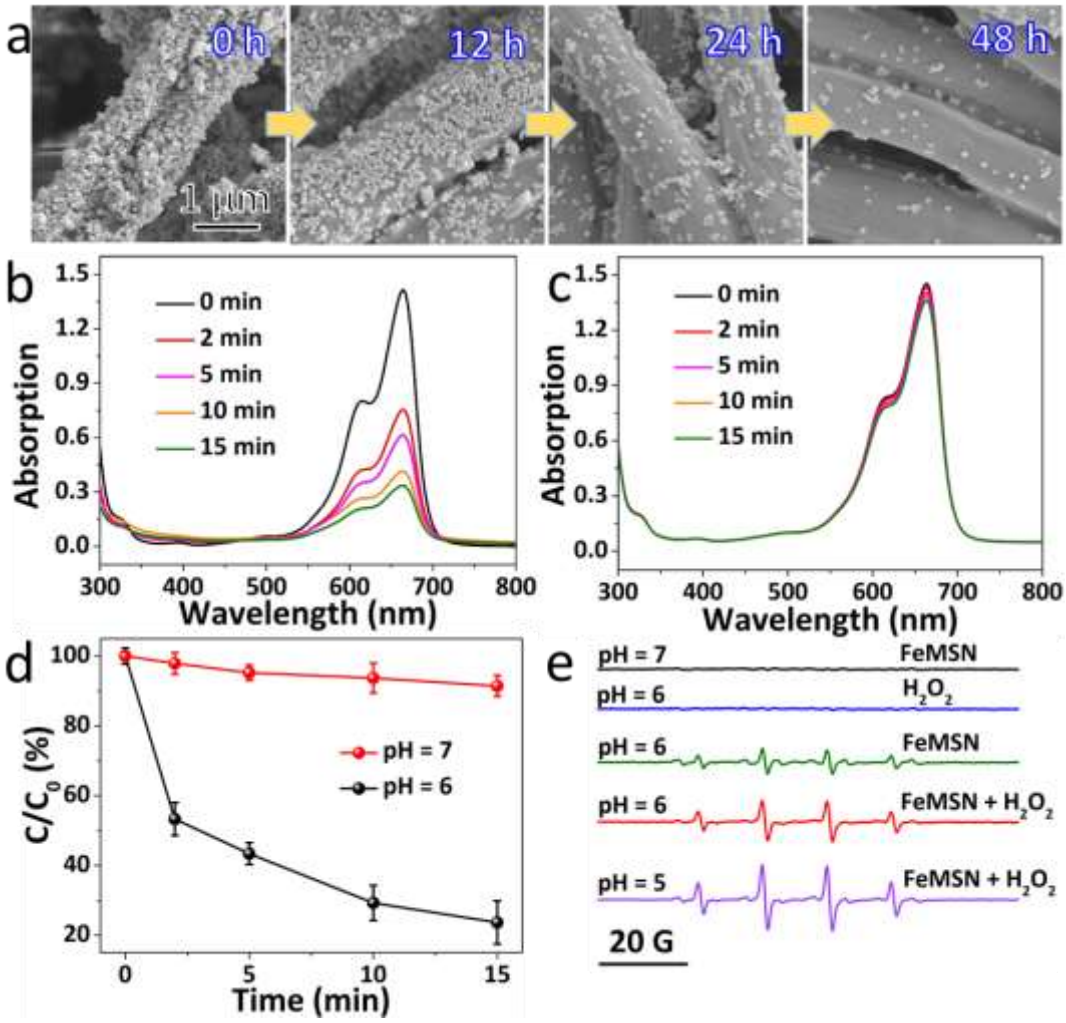

Fig. 3 (a) SEM images of FeMSN@PG fibre immersed in aqueous solution with pH = 6 for 12 h, 24 h and 48 h respectively; (b), (c) UV-Vis spectra of MB after treated with FeMSN (200 μg/mL) for 15 min at pH = 6 and pH = 7, respectively; (d) MB degradation efficiency by FeMSN (200 μg/mL) at pH = 6 and pH = 7; (e) ESR (electron spin resonance) spectra of different reaction systems with DMPO as the spin trap.

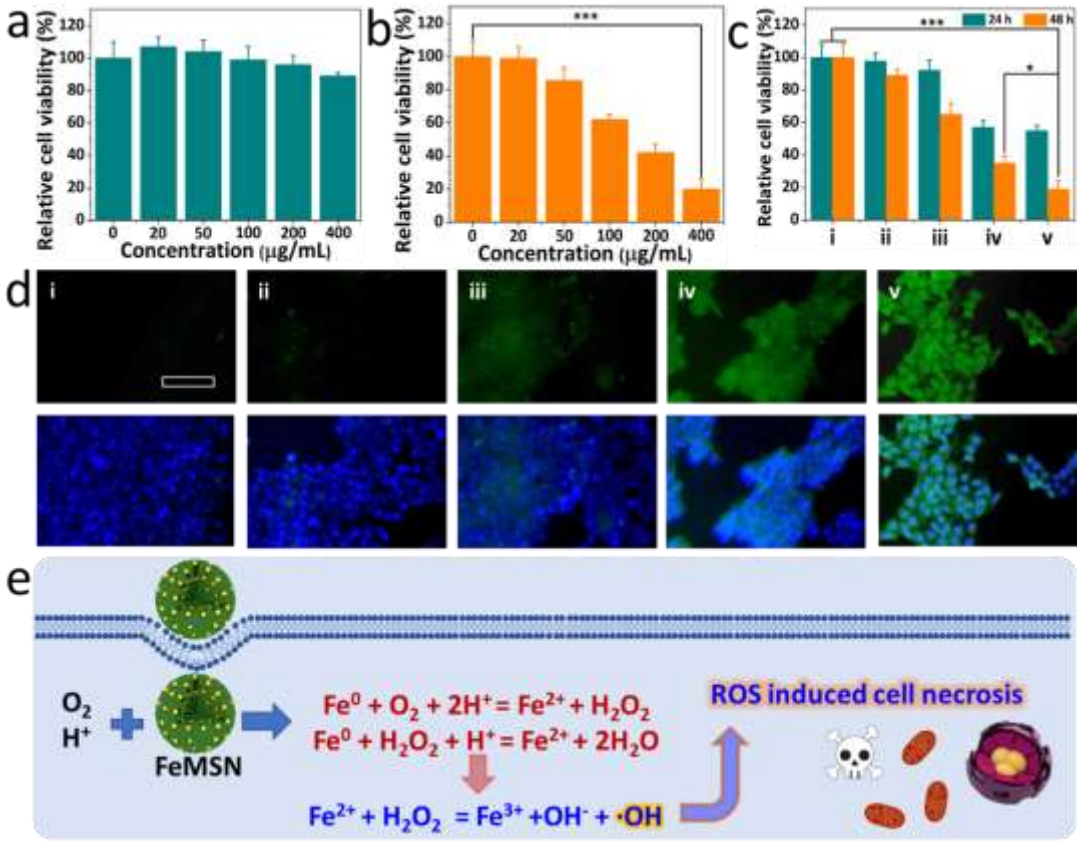

Fig. 4 (a) Relative cell viability of 7702 cells incubated with FeMSN@PG fibre for 24 h; (b) relative cell viability of 4T1 cells incubated with FeMSN@PG fibre of different concentration at pH = 6 for 48 h; (c) relative cell viability, (d) DCFH fluorescent images and merged images of 4T1 cells incubated with i: pure culture medium, ii: FeMSN@PG fibre, iii: FeMSN@PG fibre with H_2O_2, iv: FeMSN@PG fibre at pH = 6 and v: FeMSN@PG fibre with H_2O_2 at pH = 6 for 5 h; (e) Schematic illustration of the cell killing mechanism achieved by FeMSN@PG fibres. Scale bars: 100 μm.

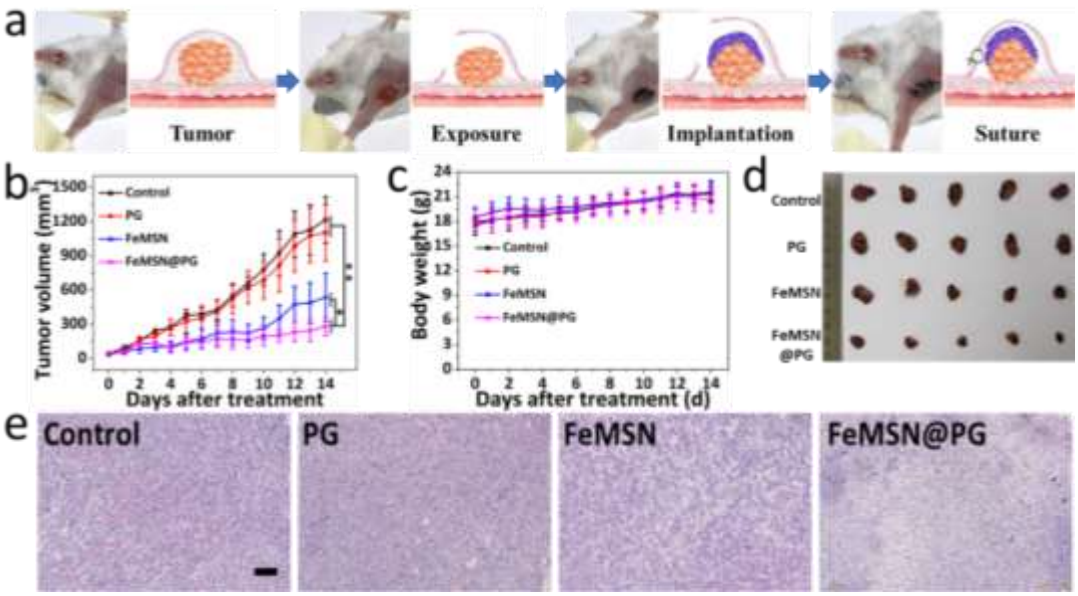

Fig. 5 (a) Digital Photograph and schematic illustration of the implantation of FeMSN@PG fibre in mice; (b) Tumor volume growth curves and (c) body weight of mice after various treatments (five mice for each group); (d) Photograph of tumors collected from different groups of mice 14 days after treatment; (e) H&E-stained tumor slices from different groups. Scale bar: 500 μm.